Hydrodynamically tunable optofluidic cylindrical microlens†‡

Xiaole Mao,[ab] John Robert Waldeisen,[a] Bala Krishna Juluri[a] and Tony Jun Huang*[ab]

Received 12th June 2007, Accepted 12th July 2007
First published as an Advance Article on the web 2nd August 2007
DOI: 10.1039/b708863a

In this work, we report the design, fabrication, and characterization of a tunable optofluidic microlens that focuses light within a microfluidic device. The microlens is generated by the interface of two co-injected miscible fluids of different refractive indices, a 5 M $CaCl_2$ solution (n_D = 1.445) and deionized (DI) water (n_D = 1.335). When the liquids flow through a 90-degree curve in a microchannel, a centrifugal effect causes the fluidic interface to be distorted and the $CaCl_2$ solution bows outwards into the DI water portion. The bowed fluidic interface, coupled with the refractive index contrast between the two fluids, yields a reliable cylindrical microlens. The optical characteristics of the microlens are governed by the shape of the fluidic interface, which can be altered by simply changing the flow rate. Higher flow rates generate a microlens with larger curvature and hence shorter focal length. The changing of microlens profile is studied using both computational fluid dynamics (CFD) and confocal microscopy. The focusing effect is experimentally characterized through intensity measurements and image analysis of the focused light beam, and the experimental data are further confirmed by the results from a ray-tracing optical simulation. Our investigation reveals a simple, robust, and effective mechanism for integrating optofluidic tunable microlenses in lab-on-a-chip systems.

Introduction

The motive to integrate tunable optical lenses within a microfluidic device stems from the promise of lab-on-a-chip systems. These systems are designed to perform a variety of on-chip biological/chemical assays, such as cell sorting,[1] single cell analysis,[2] and single molecule detection,[3] all of which will benefit from adaptive optical detection systems. While pumps, valves, and switches have been successfully integrated into lab-on-a-chip systems to allow flexible on-chip sample manipulation,[2,4] many critical components for optical detection still remain off-chip.[5] Therefore, in the past decade there has been tremendous interest in the development of on-chip adaptive optical components, especially tunable lenses. In-plane polydimethylsiloxane (PDMS) lenses have been demonstrated to increase the excitation light intensity in neighboring microfluidic channels and chambers during optical detection processes.[6–10] Although these lenses can be easily integrated within microfluidic devices, they share the common disadvantage that the geometries of these lenses are permanently fixed, as dictated by the fabrication process. Therefore, such lens designs lack the necessary mechanism to dynamically adjust focal length by reconfiguring the lens profile.

Tunable lenses that alter the focal length through deformation of the lens profile offer significant advantages in terms of functionality and versatility. Due to its unlimited deformability, liquid is a desirable medium for tunable lenses. A commonly used technique is to seal liquid in a microchamber with an elastic membrane. The curvature of the membrane can be altered by hydraulic pressure[11–15] or by applying a mechanical actuation directly onto the membrane.[16] Another type of tunable liquid lens operates by manipulating the interface between immiscible fluids (*i.e.*, water–oil or water–air). A variety of tuning mechanisms based on electrowetting,[17] stimuli-responsive hydrogels,[18] and redox surfactants[19] have been demonstrated. Unfortunately, complex fabrication procedures are often required to incorporate the tuning mechanism into these lenses. Furthermore, as most of these tunable lenses only allow focusing of light in the direction perpendicular to the device substrate, extra assembly steps are necessary to integrate these lenses with other microfluidic components. These disadvantages ultimately hinder the applicability of integrating the current tunable lenses into on-chip optical systems.

The shortcomings of the above-mentioned lenses call for the development of microlenses that can be conveniently tuned, simply fabricated, and seamlessly integrated with other microfluidic components. Recent developments in optofluidics[20–25] (the combination of microfluidics and optics) have created prospective possibilities toward the obtainment of this goal. In optofluidic devices, optics can be built entirely out of liquids and one can easily change the optical properties of the device by manipulating fluid flows.[5] Such advantages enable fabrication and tuning of purely fluidic, adaptive optical components within microfluidic devices. An intriguing example of one such device is the liquid–liquid (L^2) waveguide,[20] whose entire structure was constructed using a sheath flow of $CaCl_2$ solution and DI water. Through the manipulation of the fluid flow rate, the core ($CaCl_2$ solution) and cladding (DI

[a]*Department of Engineering Science and Mechanics, The Pennsylvania State University, University Park, PA, 16802, USA. E-mail: junhuang@psu.edu; Fax: +1-814-865-9974; Tel: +1-814-863-4209*
[b]*Department of Bioengineering, The Pennsylvania State University, University Park, PA, 16802, USA*

† Electronic supplementary information (ESI) available: Additional simulation and experiment results. See DOI: 10.1039/b708863a
‡ The HTML version of this article has been enhanced with colour images.

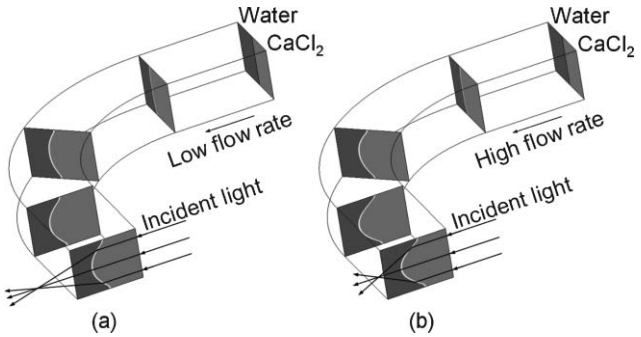

Fig. 1 The mechanism of the hydrodynamically tunable optofluidic cylindrical microlens. $CaCl_2$ solution bows outward into water due to the centrifugal effect induced in the curve. Shorter focal length is obtained after flow transitions from (a) a low flow rate to (b) a high flow rate.

water) can be hydrodynamically reconfigured to allow flexible on-chip manipulation of light.

In this work, we demonstrate a hydrodynamically tunable optofluidic microlens that can be conveniently fabricated by the standard soft lithography technique and allows variable focusing of light within a microfluidic device. The mechanism of the optofluidic tunable microlens is shown in Fig. 1. The microlens is constructed from two fluids with different refractive indices, 5 M $CaCl_2$ solution (n_D = 1.445) and DI water (n_D = 1.335). Both fluids are injected into a 90-degree microfludic curve. The adjacent injection of both miscible fluids results in an optically smooth, nearly vertical interface, due to the laminar flow that dominates in microfluidic channels. Upon entering the curve, the fluid experiences a centrifugal force along the curved trajectory. The fluid flowing in the middle of the channel (where the flow velocity is the highest) experiences a higher centrifugal force than the surrounding flow. As a result, a pair of secondary counter-rotating vortices (Dean vortices) located in the upper and lower half of the cross-sectional plane of the channel is induced. The secondary vortical flow perturbs the fluidic interface, pulling the fluid in the middle of channel towards the outer channel wall and sweeping the fluid at the top and bottom of the channel towards the inner channel wall.[26–28] Consequently, the originally flat fluidic interface bows outward, creating a cylindrical microlens. The magnitude of overall centrifugal effect or ''interface bowing'' is determined by the ratio of inertial and centrifugal force to viscous force.[27] Therefore, the shape of the fluidic interface, hence the optical characteristic of the cylindrical microlens, can be conveniently altered by changing the flow rate. Higher flow rates generate a microlens with greater curvature and hence shorter focal length. Once the fluids exit the 90-degree curve, the lens profile can be considered static, before the distortion caused by diffusion and gravity starts to play a significant role.

This paper presents a detailed study of the design, fabrication, and characterization of the hydrodynamically tunable optofluidic cylindrical microlens. A computational fluid dynamics (CFD) model is developed and experimentally validated to study the dynamic profile of the tunable microlens. The focusing effect is characterized, both experimentally and numerically, through intensity measurements

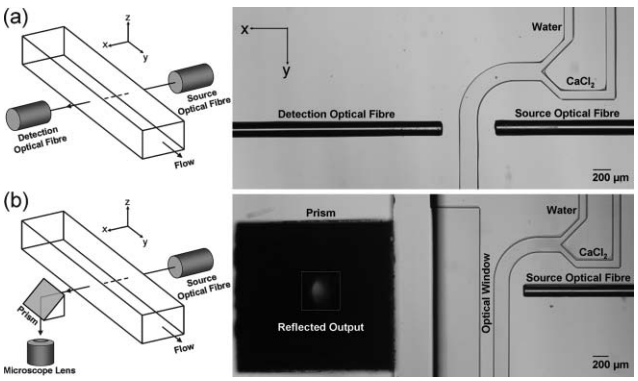

Fig. 2 (a) Device for the quantitative intensity analysis of the focused light. (b) Device for the image analysis of the focused light.

and image analysis of the focused light beam and a ray-tracing simulation. Through these experimental and numerical characterizations, we prove a simple, robust, and effective mechanism for integrating tunable optofluidic microlenses into lab-on-a-chip systems.

Methods

Device fabrication and experimental procedure

Two separate devices were designed and fabricated for microlens characterization. The first (Fig. 2a) was used for quantitative intensity analysis during the light-focusing process. This device utilized a source optical fibre connected to a halogen lamp and a detection fibre linked to a UV-Visible spectrometer (Ocean Optics). Ocean Optics SpectraSuite™ software was employed to monitor the light intensity change during the focusing process. The second device (Fig. 2b) was used for the image analysis of the focused light. This design replaced the previous detection optical fibre with an optical window that allowed the focused light beam to traverse with minimum scattering. A 2 mm × 2 mm 90-degree prism (Edmund Optics) adjacent to the optical window reflected the light beam downward[29] into the lens of an inverted optical microscope (Nikon TE 2000U), and a CCD camera (Photometrics) captured the dynamic transitions of the light spot during the focusing process. Image analysis was performed with ImageJ[30] and OriginLab® software.

The main channels in both devices were 200 μm wide and 155 μm deep. The 5 M $CaCl_2$ solution and DI water were co-injected into the main channel through two entry channels positioned at a 90-degree separation angle. A 90-degree curve with a mean radius of 500 μm was located 300 μm downstream from the converging point of the two entry channels. To enable precise positioning, optical fibres (Ocean Optics, N.A. = 0.22 ± 0.02) were inserted into guide channels with similar dimensions (155 μm × 155 μm). The guide channels were located 200 μm from the main channel and 100 μm downstream from the exit of the 90-degree curve. The optical fibres had an outer diameter of 155 μm and an inner core diameter of 50 μm.

The devices were fabricated from PDMS using the standard soft lithography protocol. The master mould for the soft lithography was made on a silicon wafer by deep reactive ion

etching (DRIE). The positive photoresist SPR-220 was lithographically patterned on the silicon wafer to act as a mask for DRIE. The etching depth on the silicon wafer was chosen to be 155 μm. After the DRIE process, the silicon wafer was subsequently coated with 1H,1H,2H,2H-perfluorooctyltrichlorosilane (Sigma Aldrich) in order to reduce damage to the channel sidewall during the following PDMS peeling steps. This silanization step is critical because a smooth PDMS channel sidewall minimizes scattering loss and ensures accurate optical measurements. Sylgard™ 184 Silicone Elastomer base and Sylgard™ 184 Silicone Elastomer curing agent (Dow Corning) were mixed at a 10 : 1 weight ratio, cast onto the silicon mould, and cured at 70 °C for 2 h. After the PDMS device was hardened, it was peeled from the mould. Inlets and outlets were drilled with a silicon carbide drill bit and the channel was subsequently sealed onto a glass slide. Polyethylene tubes were then inserted into the inlets and outlets to connect the device to syringe pumps (KD scientific). Epoxy was used to ensure proper sealing of the device.

The 5 M $CaCl_2$ solution was prepared by dissolving $CaCl_2$ salt (J.T. Baker) in DI water. The $CaCl_2$ solution and DI water were co-injected through two separate entry channels at a 1 : 1 flow rate ratio using syringe pumps. Confocal microscopy was performed on an Olympus Fluoview 300 system to reveal the full three-dimensional (3D) architecture of the fluidic interface. For the confocal microscopy experiments, DI water was dyed with 50 μM fluorescein and co-injected with the 5 M $CaCl_2$ solution. Z-stacks of fluorescent images scanned at 5 μm intervals were collected and processed by Fluoview 300 software to render 3D architectures of water flows.

Numerical simulations

A finite-volume based commercial package, CFD-ACE+ (ESI-CFD, U.S.A), was used to conduct CFD simulations. A portion of the microlens device, the 90-degree curve and adjacent straight channels (300 μm long) at both ends, was employed in our model. The computational model was divided in 40 × 16 × 100 mesh sections in the width, height, length direction, respectively, resulting in a total number of 64 000 computational grids to ensure accurate simulation results. The built-in flow and chemistry modules were used to simulate the fluid flow and mass transport inside the device. An additional user-subroutine code was developed in-house to couple the viscosity and density of the solution with variable $CaCl_2$ concentrations in the CFD simulation.

Optical simulation of the focusing process was conducted using an in-house developed ray-tracing code written in MATLAB®. Lens profiles resulting from CFD simulations at different flow rates were fitted with 8th order polynomials and each polynomial profile was discretized into small linear elements. Snell's law of refraction was employed to calculate the directional change of each input ray while travelling across these segments. The refraction of light at PDMS (n_D = 1.40) sidewalls were also taken into consideration in the simulation.

Result and discussions

The 3D architecture of the optofluidic microlens at the flow rates of 100 μl min^{-1}, 150 μl min^{-1}, and 250 μl min^{-1} are shown in Fig. 3a–c. These images, obtained by confocal microscopy, allow for the direct visualization of the cross-sectional profile of the fluidic interface. The CFD simulations of the 3D architecture at the corresponding flow rates are shown in Fig. 3d–f, indicating an excellent match with the experimental observation. Due to the nature of our optofluidic microlens (miscible fluids with unequal densities), the lens profile is subjected to the influence of diffusion and gravity after prolonged travelling time in the microchannel.[20,21] However, no significant distortion of the lens profile was observed in the confocal microscopy measurement region, as the travelling time for the fluids in this region is in the millisecond range. The position of the optical axis is stable at the different flow rates. This is important as even the slight change of optical axis position will affect the following optical detection.

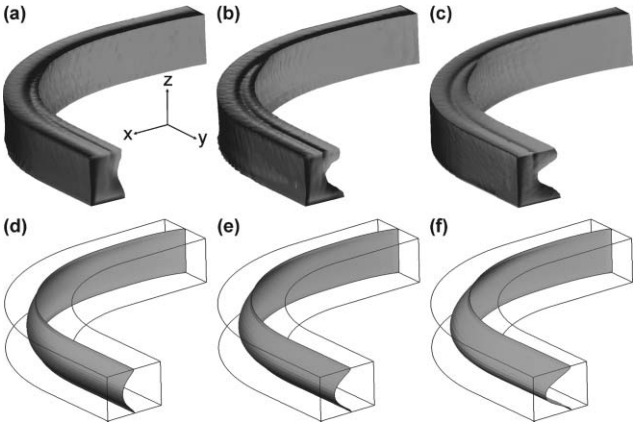

Fig. 3 The 3D architectures of water flow obtained with confocal microscopy at the flow rates of (a) 100 μl min^{-1}, (b) 150 μl min^{-1}, and (c) 250 μl min^{-1}. Images in (d–f) show the corresponding CFD-simulated 3D fluidic interfaces (isosurface of $CaCl_2$ concentration = 2.5 M).

Fig. 3 reveals that our CFD model matches well with the experimental results under a variety of flow conditions. Yamaguchi *et al.* reported a numerical study of the fluidic interface in microfluidic hairpin curves.[26] Their simulations investigated water and a dilute fluorescein solution, two fluids with almost the same density and viscosity. In our study, however, DI water and 5 M $CaCl_2$ solution are significantly different in their hydrodynamic properties. The viscosity and density of the $CaCl_2$ solution at 25 °C are approximately 7.9 mPa·s and 1390 kg m^{-3}, 890% and 39% higher than those of water.[31] Furthermore, the dependence of density and viscosity on $CaCl_2$ concentration results in a coupling issue between fluid flow and mass transport. As previously mentioned the centrifugal effect is determined by the relative importance of the inertial and centrifugal force to viscous force. Therefore, the variation of density and viscosity should be taken into consideration for the numerical simulation. A user-subroutine code was developed to calculate and update the viscosity and density of the two fluids within each computational grid during every iteration. We found that only when we thoroughly consider the $CaCl_2$ concentration-dependent hydrodynamic properties (viscosity and density) can our simulation results faithfully duplicate experimental data.

Quantitative analysis of the focused light intensity was performed on the microlens device shown in Fig. 2a. Normalized light intensity was measured by the detection optical fibre for flow rates ranging from 0 μl min^{-1} to 400 μl min^{-1}, at 50 μl min^{-1} intervals (Fig. 4a). As the flow rate was increased from 0 to 250 μl min^{-1}, the light focused into the detection fibre intensified as a result of the increasing microlens curvature and the focal plane approaching the aperture of the detection fibre (shorter focal length). A linear correlation could also be extrapolated among the detection intensity and flow rates between 50 μl min^{-1} and 200 μl min^{-1}. Light intensity subsequently decreased after reaching the maximum intensity at the flow rate of 250 μl min^{-1}. This phenomenon occurred because the light was focused before reaching the aperture of the detection fibre (over-focused). Simulation results of the microlens profile for flow rates ranging from 50 μl min^{-1} to 400 μl min^{-1}, at 50 μl min^{-1} intervals, are shown in the inset of Fig. 4a. Interestingly, all the lens profiles intersected at two points, resulting in virtually pinned fluidic interfaces. The distance between the two pinned points of intersection was approximately 60 μm.

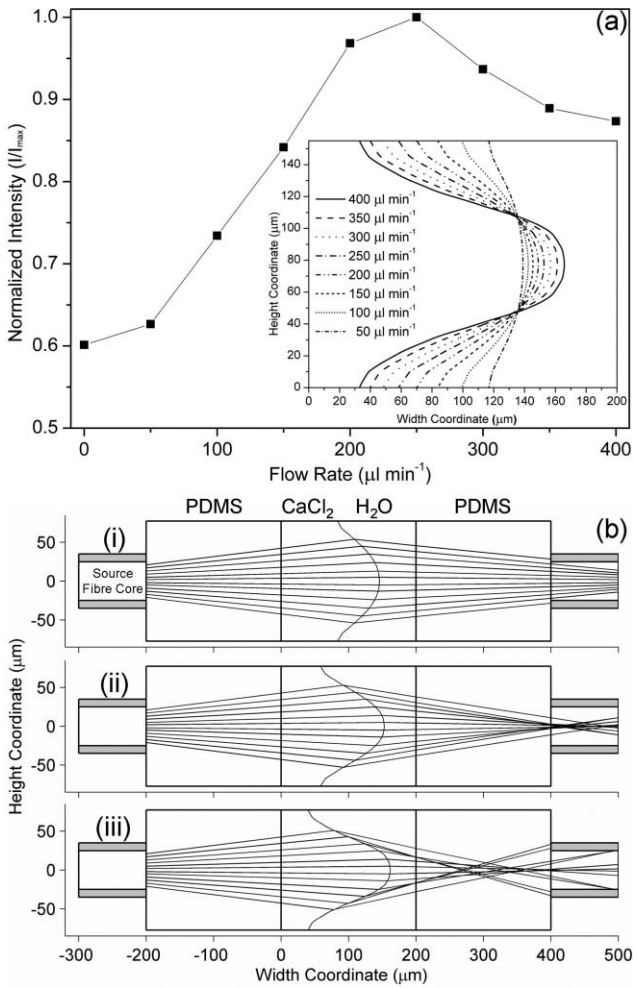

Fig. 4 (a) Normalized light intensity measured for flow rates ranging from 0 μl min^{-1} to 400 μl min^{-1}, at 50 μl min^{-1} intervals. Inset: the CFD-simulated results of the fluidic interface at respective flow rates (except for 0 μl min^{-1}). (b) Ray-tracing simulation reveals three different focusing patterns: (i) under-focused mode at the flow rate of 150 μl min^{-1}, (ii) well-focused mode at the flow rate of 250 μl min^{-1}, and (iii) over-focused mode at the flow rate of 350 μl min^{-1}.

Using the simulated lens profiles, we performed a ray-tracing simulation to calculate the focal length of the optofluidic microlens at different flow rates, and the results are shown in Fig. 4b. The numerical aperture of the fibre is 0.22 in air, equivalent to 0.16 in PDMS (n_D = 1.4), which causes the incident angle of the input beam to vary from 0 to approximately 9.0° (acceptance angle of fibre in PDMS). A cone-shape divergent light source was employed to simulate the input beam of the fibre. Three different flow rates (150, 250, and 350 μl min^{-1}) resulted in three focusing patterns representing (i) under-focused, (ii) well-focused, and (iii) over-focused configurations. From (i) to (ii), the increase of the flow rate resulted in a decrease of focal length, causing the focal plan to approach the aperture of the detection fibre. The increased focusing power of the lens causes more of the divergent incident beams to bend into the detection fibre. This corresponds to the increase of detection intensity between 150 and 250 μl min^{-1}, as shown in Fig. 4a. At the flow rate of 250 μl min^{-1}, most of the incident light beams are well focused near the fibre aperture (ii), corresponding to the maximum intensity observed in the experiment. From (ii) to (iii), as shown in the simulation, over-focusing of the light causes the incident light beams to focus before reaching the fibre aperture and subsequently diverge. Therefore, less light is coupled into the optical fibre, resulting in a decrease of detection intensity observed in Fig. 4a.

It is worth mentioning the variation in the incident angles of input light beams will result in different focal point positions (aberration). We have conducted a second ray-tracing optical simulation with perfectly parallel input light beams (Fig. 1S in the ESI†). Much less aberation is oberserved in this case. In the future study, a well colimated light source (such as a laser) would be more suitable.

The image analysis of the focused light was performed on the second microlens device (Fig. 2b) that utilized the optical window and 90-degree prism. The flow rate was initially set at 250 μl min^{-1}, as this rate yielded the well-focused pattern in the ray-tracing simulation. The microscope lens was then fixed at a position where the sharpest image of the focused light spot at the flow rate of 250 μl min^{-1} could be captured. The flow rate was then adjusted to meet different experimental conditions. Fig. 5a–c depict the images of the light spot obtained at the flow rates of 0 μl min^{-1}, 150 μl min^{-1}, and 250 μl min^{-1}, respectively. The focusing effect is evident from the observed changes in the shape and intensity of the light spot. Additionally, image analysis at the corresponding flow rates was performed, as shown in Fig. 5d–f. These figures depict an intensity increase as the light spot is focused, reaffirming the quantitative data presented in Fig. 4.

We note from the experimental results in Fig. 5 that the optofluidic microlens suffers from a certain degree of aberration. We attribute the observed aberration to two causes: first, the source light from the optical fibre is not a perfectly collimated monochromatic light beam (also shown in the ray-tracing simulation in Fig. 4a); second, the lens profile is closer to parabolic geometry, rather than circular geometry.

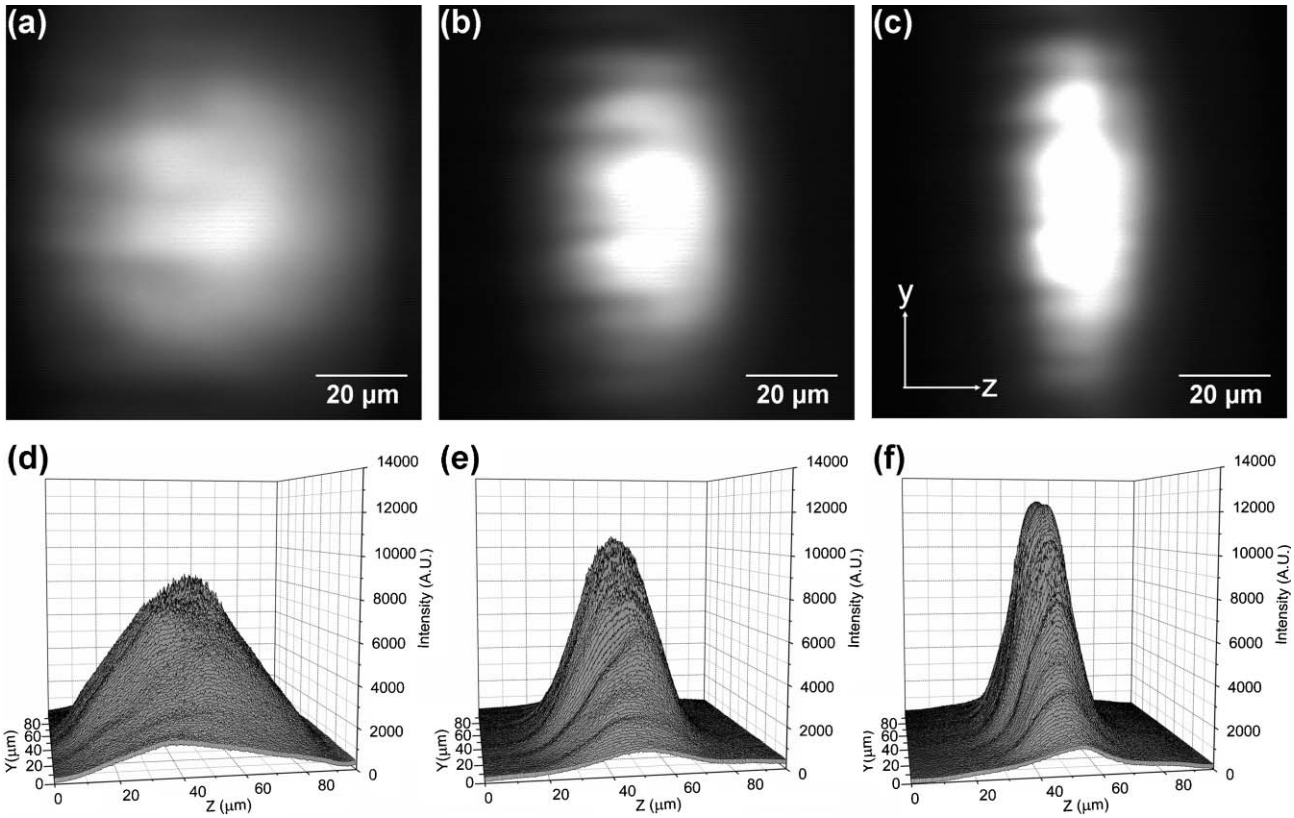

Fig. 5 Microscopic images of the source optical fibre output at (a) 0 μl min^{-1}, (b) 150 μl min^{-1}, and (c) 250 μl min^{-1}. Images (d), (e), and (f) show the 3D intensity plot for the corresponding microscopic images.

However, if the lens curvature is small enough, the parabolic lens could be approximated as circular-shaped with negligible error.[32] It is expected that the use of miscible fluids with higher refractive index contrasts (*i.e.*, ethanol and high-refractive-index oil) could achieve a microlens with a smaller curvature, and hence less aberration.

Finally, the stability and switching speed of our optofluidic microlens was tested (Fig. 2S in the ESI†). The results illustrate the stable and repeatable switching nature of our optofluidic microlens, thus proving the robustness of the tuning mechanism.

Conclusions

This study introduces a technique for the creation of a hydrodynamically tunable optofluidic cylindrical microlens that can be conveniently fabricated and integrated within a microfluidic device. The investigation also reveals a mechanism in which light can be focused at different focal planes by simply changing the flow rates of the two miscible fluids. Such an in-plane tunable cylindrical microlens is particularly attractive because it can be easily integrated with the currently existing lab-on-a-chip devices[1,2,33] to create fully integrated optical detection systems for applications, such as flow cytometry, single molecule detection, and the study of chemical kinetics. We envision that by combining our tunable microlenses with other optofluidic devices, such as the L^2 waveguide[19] and L^2 light source,[23] it is possible to realize all-inclusive, all-liquid on-chip adaptive optical systems for numerous lab-on-a-chip applications.

Acknowledgements

The authors thank Jinjie Shi for his help on device fabrication, and Ashley Colletti, Vincent K.S. Hsiao, Yuebing Zheng, and Daniel Ahmed for their help in preparing the manuscript. This research was supported in part by the start-up fund provided by the Pennsylvania State University, the Grace Woodward Grants for Collaborative Research in Engineering and Medicine, and the NSF NIRT grant (ECCS-0609128). Components of this work were conducted at the Penn State node of the NSF-funded National Nanotechnology Infrastructure Network.

References

1 M. M. Wang, E. Tu, D. E. Raymond, J. M. Yang, H. Zhang, N. Hagen, B. Dees, E. M. Mercer, A. H. Forster, I. Kariv, P. J. Marchand and W. F. Butler, *Nat. Biotechnol.*, 2005, **23**, 83–87.
2 B. Huang, H. Wu, D. Bhaya, A. Grossman, S. Granier, B. K. Kobilka and R. N. Zare, *Science*, 2007, **315**, 81–84.
3 T.-H. Wang, Y. Peng, C. Zhang, P. K. Wong and C.-M. Ho, *J. Am. Chem. Soc.*, 2005, **127**, 5354–5359.
4 T. Thorsen, S. J. Maerkl and S. R. Quake, *Science*, 2002, **298**, 580–584.
5 D. Psaltis, S. R. Quake and C. Yang, *Nature*, 2006, **442**, 381–386.
6 J. Godin, V. Lien and Y.-H. Lo, *Appl. Phys. Lett.*, 2006, **89**, 061106.
7 S. Camou, H. Fujita and T. Fujii, *Lab Chip*, 2003, **3**, 40–45.

8 A. Llobera, R. Wilke and S. Buettgenbach, *Lab Chip*, 2004, **4**, 24–27.
9 Z. Wang, J. El-Ali, M. Engelund, T. Gotsaed, I. R. Perch-Nielsen, K. B. Mogensen, D. Snakenborg, J. P. Kutter and A. Wolff, *Lab Chip*, 2004, **4**, 372–377.
10 J. Seo and L. P. Lee, *Sens. Actuators, B*, 2004, **99**, 615–622.
11 L. Pang, U. Levy, K. Campbell, A. Groisman and Y. Fainman, *Opt. Express*, 2005, **13**, 9003–9013.
12 N. Chronis, G. Liu, K.-H. Jeong and L. Lee, *Opt. Express*, 2003, **11**, 2370–2378.
13 D.-Y. Zhang, V. Lien, Y. Berdichevsky, J. Choi and Y.-H. Lo, *Appl. Phys. Lett.*, 2003, **82**, 3171–3172.
14 S. W. Lee and S. S. Lee, *Appl. Phys. Lett.*, 2007, **90**, 121129.
15 A. Werber and H. Zappe, *Appl. Opt.*, 2005, **44**, 3238–3245.
16 H. Ren and S.-T. Wu, *Appl. Phys. Lett.*, 2005, **86**, 211107.
17 S. Kuiper and B. H. W. Hendriks, *Appl. Phys. Lett.*, 2004, **85**, 1128–1130.
18 L. Dong, A. K. Agarwal, D. J. Beebe and H. Jiang, *Nature*, 2006, **442**, 551–554.
19 C. A. Lopez, C.-C. Lee and A. H. Hirsa, *Appl. Phys. Lett.*, 2005, **87**, 134102.
20 D. B. Wolfe, R. S. Conroy, P. Garstecki, B. T. Mayers, M. A. Fischbach, K. E. Paul, M. Prentiss and G. M. Whitesides, *Proc. Natl. Acad. Sci. U. S. A.*, 2004, **101**(34), 12434–12438.
21 D. V. Vezenov, B. T. Mayers, D. B. Wolfe and G. M. Whitesides, *Appl. Phys. Lett.*, 2005, **86**, 041104.
22 D. Erickson, T. Rockwood, T. Emery, A. Scherer and D. Psaltis, *Opt. Lett.*, 2006, **31**, 59–61.
23 P. Domachuk, C. Grillet, V. Ta'eed, E. Magi, J. Bolger, B. J. Eggleton, L. E. Rodd and J. Cooper-White, *Appl. Phys. Lett.*, 2005, **86**, 024103.
24 P. Domachuk, I. C. M. Littler, M. Cronin-Golomb and B. J. Eggleton, *Appl. Phys. Lett.*, 2006, **88**, 093513.
25 X. Heng, D. Erickson, L. R. Baugh, Z. Yaqoob, P. W. Sternberg, D. Psaltis and C. Yang, *Lab Chip*, 2006, **6**, 1274–1276.
26 Y. Yamaguchi, F. Takagi, K. Yamashita, H. Nakamura, H. Maeda, K. Sotowa, K. Kusakabe, Y. Yamasaki and S. Morooka, *AIChE J.*, 2004, **50**, 1530–1535.
27 A. P. Sudarsan and V. M. Ugaz, *Lab Chip*, 2006, **6**, 74–82.
28 P. B. Howell, Jr., D. R. Mott, J. P. Golden and F. S. Ligler, *Lab Chip*, 2004, **4**, 663–669.
29 J. Leyton-Mange, S. Yang, M. H. Hoskins, R. F. Kunz, J. D. Zahn and C. Dong, *J. Biomech. Eng.*, 2006, **128**, 271–278.
30 NIH, http://rsb.info.nih.gov/ij/.
31 H.-L. Zhang, G.-H. Chen and S.-J. Han, *J. Chem. Eng. Data*, 1997, **42**, 526–530.
32 H. Ren, D. Fox, P. A. Anderson, B. Wu and S.-T. Wu, *Opt. Express*, 2006, **14**, 8031–8036.
33 S. A. Pabit and S. J. Hagen, *Biophys. J.*, 2002, **83**, 2872–2878.

